Passive control of temperature distribution in cancerous tissue during photothermal therapy using optical phase change nanomaterials

Yatao Ren,[a, c] Qin Chen,[a] Huaxin Li,[a] Hong Qi,[a, b, *] Yuying Yan,[c, d, *]

a School of Energy Science and Engineering, Harbin Institute of Technology, Harbin 150001, P. R. China

b Key Laboratory of Aerospace Thermophysics, Ministry of Industry and Information Technology, Harbin 150001, P. R. China

c Faculty of Engineering, University of Nottingham, University Park, Nottingham NG7 2RD, UK

d Research Centre for Fluids and Thermal Engineering, University of Nottingham Ningbo China, Ningbo 315100, China

* Email: qihong@hit.edu.cn (H. Qi); yuying.yan@nottingham.ac.uk (Y. Yan)

Abstract: Thermal therapy is a very promising alternative treatment for benign tumor, in which the temperature control is a key issue to avoid unwanted thermal damage of healthy tissue. However, the active temperature control methods usually require the assistance of real-time and accurate temperature monitoring devices. Even though, the lag of temperature control is inevitable. Therefore, in the present work, a passive control method is proposed to improve the uniformity of temperature distribution inside tumorous tissue during laser induced thermal therapy (LITT). Optical phase change nanoparticles (O-PCNPs) are utilized to replace the commonly used noble

metal nanoparticles to enhance and adjust the localized light absorption in tumor. In the early stage of LITT, the O-PCNPs is used to improve the specific absorption rate in the targeted region. However, after the local temperature reaches a certain level (phase transition temperature), the O-PCNPs convert from amorphous state to crystalline state. By carefully selecting the size, shape, and laser wavelength, the absorption cross section of O-PCNPs could drop dramatically after phase transition. Therefore, in the high temperature zone the local temperature increasing rate reduces due to the reduction of local heat generation rate. On the contrary, the temperature increasing rate rises in the low temperature zone since more energy is transferred to the deeper tissue. In the present work, results show that SiO_2@VO_2 nanoshells can be applied as thermal contrast agents to improve the temperature uniformity in tumor during LITT.

Keywords: Thermal therapy; optical phase change nanoparticles; light and heat transfer; passive control; VO_2

1. Introduction

Due to its minimal- or non-invasive nature and free of side effect, tumor thermal therapy has been regarded as one of the most promising techniques that can be applied to the treatment of early stage tumors, especially for the patients who are not suitable for radiotherapy, chemotherapy, or surgery due to their physical conditions [1-7]. During thermal therapy, the most essential step is to keep the cancerous tissue in hyperthermia condition for a certain period of time. Hyperthermia is usually defined as keeping the targeted areas in a temperature range between 41 to 47 ℃ for tens of minutes [8] or higher temperature for shorter time, which can lead to the death of cancer cells. In the meantime, due to the heat diffusion, the surrounding healthy tissues are also inevitably

suffered from hyperthermia [1]. Therefore, the real-time and precise control of temperature distribution in targeted areas is of great importance to minimize the damage of the healthy tissue. Despite a mass of efforts that have been put into this field, precise temperature control of cancerous tissue, remains to be a big challenge.

To confine the hyperthermia state inside a desired region, the temperature distribution should be monitored first. Therefore, the real-time temperature monitoring devices are very important accessory techniques to provide guidance for the employment of thermal dosage and to provide real-time temperature correction for the prediction of the numerical model [9]. The temperature then can be controlled easily by simply adjusting the power of laser, ultrasound, or microwave, depending on the specific heating strategy applied. Various techniques have been proposed to monitor the temperature in certain points or distribution in the region of interest, such as thermocouples [10], near-infrared thermal imaging [11, 12], ultrasound thermal mapping [13, 14], photoacoustic temperature measurement [9, 15], magnetic resonance temperature imaging [16-18]. Recently, a temperature label, i.e., temperature feedback upconversion nanoparticle, was applied in photothermal therapy to display the temperature in targeted cells directly through luminescence image [19]. Despite the abovementioned temperature monitoring methods, a fully understanding of the light and heat transfer process in biological tissue to predict the temperature distribution during thermal therapy is also very important [20-31]. However, this is very difficult to achieve due to the complex situations in living systems, such as the variation of blood perfusion and thermophysical properties of tissue.

Most of the abovementioned techniques can be characterized as active control methods, which means the thermal dosage is adjusted during the treatment according to the feedbacks of temperature measurement or simulation results. The performance of the active methods deeply

relies on the accuracy of the measurement equipment or numerical methods. Considering the complexity of heat diffusion in human body, all the active methods inevitably suffer from low accuracy and time-delay effect. Therefore, other alternative methods need to be provided. As far as we know, the passive temperature control method in thermal therapy has not been reported to date. Herein, passive temperature control means that the temperature in the targeted area does not have or rarely needs to be controlled by external devices such as modulating the power of external heat sources. In the present work, we proposed the concept of using optical phase change nanomaterials to provide localized heat sources in photothermal therapy instead of noble metal nanoparticles for the first time. Optical phase change materials (O-PCMs), such as VO_2, refer to one type of materials that exhibit obvious optical properties change when undergo a solid-state phase transition induced by temperature change [32]. O-PCMs are widely applied in areas like reconfigurable metasurface, optical switching, and photonic memories [32-36], but not thermal therapy. It is known that nanoparticles are served as nanosources of heat to heat the cancerous tissue selectively during thermal therapy [6, 37, 38]. Therefore, the temperature of cancerous area will keep increasing if not controlled properly. Then the surrounding healthy tissue may be damaged due to heat diffusion. The basic concept of the proposed method is that when the temperature of the nanoparticles reaches the phase transition temperature of the O-PCMs, the dielectric constants of the nanomaterial will change accompanying with the phase transition process. Ideally, by adjusting the size, shape, and component of the nanomaterials, the effect can be achieved that after the phase transition, the absorption cross section of the nanoparticle will significantly decrease, and therefore to minimize the heating rate in the high temperature region and increase the temperature uniformity in tumor.

In the present work, the optical properties of VO_2 and Ge-Sb-Te (GST) nanospheres, two widely used O-PCMs are investigated. Moreover, to improve biocompatibility, reduce toxicity, and enable easy functionalization, the nanoparticles can be coated with SiO_2 shells [39-42]. Therefore, the influence of the SiO_2 shell thickness on the performance of the phase transition nanomaterials is also investigated. The remainder of this work is organized as follows. Section 2 introduces the basic principle of discrete dipole approximation (DDA) and the light and heat transfer model in biological tissue. Section 3 presents the main results and discussions including the optical properties of VO_2 and GST nanospheres, the specific absorption rate and temperature distributions during laser induced thermal therapy considering the phase change of embedded nanoparticles. Finally, main conclusions are given in Section 5.

2. Methods

2.1. Discrete dipole approximation

In the present work, the optical properties of nanoparticles are calculated by DDA. The basic principle of DDA is to discretize nanoparticles into a cubic array of virtual *N*-point dipoles. Therefore, it is convenient for the calculation of the optical properties of arbitrary shaped particles. The polarization of the *j*th dipole can be expressed as $\mathbf{P}_j = \alpha_j \mathbf{E}_j$, where α_j is the polarizability of the *j*th dipole and $\mathbf{E}_j$ is the electric field in position $\mathbf{r}_j$, which can be obtained by [43, 44]:

$$\mathbf{E}_j = \mathbf{E}_j^{\mathrm{inc}} - \sum_{k \neq j} \mathbf{A}_{jk} \mathbf{P}_k \tag{1}$$

where $\mathbf{E}_j^{\mathrm{inc}}$ is the incident electric field, which is given by $\mathbf{E}_j^{\mathrm{inc}} = \mathbf{E}_0 \exp\left(ik \cdot \mathbf{r}_j - i\omega t\right)$, in which $\mathbf{E}_0$ is the amplitude of the electric field intensity and k can be expressed as ω/c, where ω and c are the angular frequency and speed of light in the medium, respectively. $\mathbf{A}_{jk}$ stands for the interaction

matrix. $\mathbf{A}_{jk}\mathbf{P}_k$ is the electric field at position $\mathbf{r}_j$, which is triggered by the dipole at position $\mathbf{r}_k$, which can be expressed as [44]:

$$\mathbf{A}_{jk}\mathbf{P}_k = \frac{\exp\left(ik\mathbf{r}_{jk}\right)}{\mathbf{r}_{jk}^3}\left\{k^2\mathbf{r}_{jk}\times\left(\mathbf{r}_{jk}\times\mathbf{P}_k\right)+\frac{\left(1-ik\mathbf{r}_{jk}\right)}{\mathbf{r}_{jk}^2}\times\left[\mathbf{r}_{jk}^2\mathbf{P}_k-3\mathbf{r}_{jk}\cdot\mathbf{P}_k\right]\right\}, \quad j\neq k \tag{2}$$

If $\mathbf{A}_{jj}$ is defined as $\mathbf{A}_{jj}=-\alpha_j^{-1}$, then the scattering problem can be described as a set of linear equations as follows:

$$\sum_{k=1}^{N}\mathbf{A}_{jk}\mathbf{P}_k=\mathbf{E}_j^{\text{inc}} \tag{3}$$

Then, the extinction, absorption, and scattering cross section can be calculated by

$$C_{\text{ext}}=\frac{4\pi k}{\left|\mathbf{E}_0\right|^2}\sum_{j=1}^{N}\text{Im}\left(\mathbf{E}_j^{\text{inc},*}\cdot\mathbf{P}_j\right) \tag{4}$$

$$C_{\text{abs}}=\frac{4\pi k}{\left|\mathbf{E}_0\right|^2}\sum_{j=1}^{N}\left[\text{Im}\left(\mathbf{P}_j\cdot\alpha_j^{-1}\cdot\mathbf{P}_j^{*}\right)-\frac{2}{3}k^3\left|\mathbf{P}_j\right|^2\right] \tag{5}$$

$$C_{\text{sca}}=C_{\text{ext}}-C_{\text{abs}} \tag{6}$$

where the superscript '*' means the conjugate function of the original variable. The corresponding extinction, absorption, and scattering efficiencies (Q_{ext}, Q_{abs}, and Q_{sca}) are the ratio of cross section and πR^2. The detailed description and mathematical formulation of DDA also can be found in Ref. [43, 44]. In the present work, the spectral optical properties of phase change materials, *i.e.* VO_2 and GST ($Ge_3Sb_2Te_6$) are studied, the dielectric function of which can be obtained in Refs. [45, 46]. The validation of the present numerical model to calculate the optical properties of nanoparticles can be found in our previous work [47].

2.2 Light and heat transfer in biological tissue embedded with nanoparticles

In the present work, the Pennes bioheat transfer equation with light induced volumetric heat source Q_r, is used to describe the heat transfer problem of nanoparticles embedded biological tissue under laser irradiation, which can be written as [1]:

$$\rho c_p \frac{\partial T}{\partial t} = k\nabla^2 T + Q_b + Q_m + Q_r \tag{7}$$

where ρ, c_p, T, and k denote density, specific heat, temperature, and thermal conductivity of the tissue, respectively. Q_m stands for volumetric metabolic heat generation rate. Q_b is the heat exchange between blood vessel and tissue matrix, which can be expressed as [48]:

$$Q_b = w_b \rho_b c_{pb} \left(T_b - T\right) \tag{8}$$

where w is the blood perfusion rate of the tissue. The subscript 'b' stands for blood.

Q_r is the radiative heat source or specific absorption rate (SAR) induced by the absorption of incident light energy by tissue matrix or embedded nanoparticles. The calculation of Q_r can be achieved by most of the commonly used numerical methods for radiative transfer in semitransparent media, such as finite volume method, finite element method, discrete coordinate method, *etc*. [49, 50]. The radiative transfer equation for semitransparent media can be expressed as [51]:

$$\mathbf{\Omega}\nabla I\left(\mathbf{s},\mathbf{\Omega}\right) + \beta I\left(\mathbf{s},\mathbf{\Omega}\right) = \frac{\mu_s}{4\pi}\int_{4\pi} I\left(\mathbf{s},\mathbf{\Omega}'\right)\Phi\left(\mathbf{\Omega}',\mathbf{\Omega}\right)d\mathbf{\Omega}' \tag{9}$$

where I is the radiative intensity in direction $\mathbf{\Omega}$ and location $\mathbf{s}$. Φ stands for the scattering phase function. Then Q_r can be expressed as:

$$Q_r = -\int_{4\pi} \mathbf{\Omega}\nabla I d\mathbf{\Omega} \tag{10}$$

It should be noted that due to the limited speed of thermal wave in biological tissue, it is more accurate to use non-Fourier heat transfer models, such as thermal wave model and dual phase lag

model [52-54], to predict the temperature distributions in biological tissue. Meanwhile, comparing with the Fourier model (Pennes bioheat transfer), the non-Fourier model is more accurate to predict thermal response for very short time lag transient problems, for example the high fluence, short laser irradiating time problems. In another word, the major discrepancies between the two models become evident when the tissue is briefly exposed to severe heat. For longer exposure times and deeper skin depths, the obtained results from both Fourier and non-Fourier model coincide with each other basically [55]. In the present work, the applied laser power density is 20 kW/m^2, which is relatively small, and the tissue is exposed to laser continuously. Therefore, the standard Pennes bio-heat transfer equation will be adequate for the present work, considering the focus of this work is to investigate the passive temperature control method using optical phase change nanomaterials. Nevertheless, further studies to investigate the non-Fourier effect in this situation is also important.

In the present work, we assume that the nanoparticles are distributed uniformly in the tissue matrix. Therefore, the optical properties of tissue embedded with nanoparticles can be calculated by:

$$\begin{cases} \beta = \beta_{\mathrm{n}} + \beta_{\mathrm{t}} \\ \mu_{\mathrm{a}} = \mu_{\mathrm{a,n}} + \mu_{\mathrm{a,t}} \\ \mu_{\mathrm{s}} = \mu_{\mathrm{s,n}} + \mu_{\mathrm{s,t}} \end{cases} \tag{11}$$

where β, μ_{a}, and μ_{s} stand for the attenuation, absorption, and scattering coefficients of tissue with nanoparticles, respectively. The subscript n and t stand for the properties correspond to nanoparticles system and tissue matrix, respectively.

Due to the high adaptability for complex geometries and ease of implementation, Monte Carlo method (MCM) has been frequently used in the field of laser tissue interaction [56, 57]. The basic principle of MCM is shown in Fig. 1. When the Monte Carlo method is applied to calculate the propagation of light in biological tissue, the first step is to decide the step size of incident photons

which must be smaller compared to the mean free path of a photon in tissue, which can be expressed as [58]:

$$\Delta s < \frac{1}{\beta} = \frac{1}{\mu_a + \mu_s} \tag{12}$$

Usually, the step size for each phonon is different to improve the efficiency of the method. The probability density function for the step size follows Beer's law, which means that the probability is proportional to $e^{-\beta_t \Delta s}$. This is achieved by generating a random number $N_{rand,1}$ evenly distributed between 0 and 1. Then the step size can be expressed as [58]:

$$\Delta s = \frac{-\ln N_{rand,1}}{\beta} \tag{13}$$

The step size Δs means the distance that a photon will travel before interacting (through absorption or scattering) with the tissue embedded with nanoparticles. Specifically, in the present work, it means that the photon will be absorbed or scattered by tissue matrix of nanoparticles after travelling for the distance Δs. The probability of interacting with tissue or matrix is proportional to their relative values of attenuation coefficients. Therefore, in the present work, this is decided by generating a new random number $N_{rand,2}$. If $N_{rand,2} > \beta_n / (\beta_n + \beta_t)$, the light is interacting with tissue. Otherwise, light is interacting with nanoparticles. It should be noted that the anisotropic scattering characteristic of nanoparticles and tissues are both taken into consideration in the present work. The scattering directions can be decided according to the corresponding scattering properties (asymmetry factor g) as follows [58]:

$$\cos\theta = \frac{1}{2g}\left[1 + g^2 - \left(\frac{1 - g^2}{1 - g + 2gN_{rand}}\right)\right] \tag{14}$$

$$\phi = 2\pi N_{rand} \tag{15}$$

where θ and ϕ are the polar angle and azimuthal angle, respectively. It should be noted that the asymmetry factors of tissue matrix and nanoparticles are different. The verification of present light and heat transfer model of in biological tissue that does not considering the influence of phase change nanoparticles can be found in our previous work [1] and will not be repeated here. More details can be found in Ref. [56-58].

Fig. 1 Flowchart of Monte Carlo method.

3. Results and Discussions

3.1 Temperature dependent optical properties of O-PCMs

As mentioned above, the function of O-PCMs is to reduce the light absorption of high temperature zone, and therefore to reduce the temperature increasing rate. Naturally, the desired nanoparticle should have an absorption efficiency that decreases dramatically when its phase changes from amorphous state to crystalline state. Therefore, a figure of merit P is proposed to evaluate the performance of the optical phase change nanoparticles (O-PCNPs), which is defined as:

$$P = \frac{Q_{\mathrm{abs}}^{\mathrm{a}} - Q_{\mathrm{abs}}^{\mathrm{c}}}{Q_{\mathrm{abs}}^{\mathrm{a}}} \times 100\% \tag{16}$$

where Q_{abs} is the absorption efficiency of nanoparticles. Superscript ‘a’ and ‘c’ represent ‘amorphous state (a-state)’ and ‘crystalline state (c-state)’, respectively. Apparently, P is the percentage reduction of Q_{abs} after phase transition. Larger P represents a smaller absorption efficiency of nanoparticle when its phase changes from amorphous state to crystalline state. Considering an ideal condition where P = 1.0, which means that the Q_{abs} of c-state nanoparticles reduce to 0, the specific absorption rate in the high temperature zone (with c-state nanoparticles)

can be minimized. Another extreme condition is $P = 0.0$, which means Q_{abs} does not change after phase transition, which is the same with the case of regular nanoparticles like gold nanoparticles. Therefore, larger P is preferred in the proposed temperature control method. It should also be noted that the value of P can be negative when Q_{abs} of c-state nanoparticle is larger than that of its a-state counterpart.

To explore the possibility of using O-PCNPs to control the temperature distribution in cancerous tissue during photothermal therapy, we first investigated the optical properties of VO_2 and GST nanospheres. It is found that when r =30 and 60 nm, the absorption efficiencies of c-state nanoparticles are always larger than those of a-state nanoparticles, which means P is always negative. Therefore, the absorption of light after phase change is increased instead of decreased. However, when the particle radius is larger than 90 nm, there will be an obvious waveband that satisfies the criteria of $P > 0.0$ (see Figs. 2-4). It can be seen that for VO_2 nanosphere, this range is from 560 to 700 nm, and for GST nanospheres, this range is from 700 to 1000 nm. Therefore, it is possible to reduce the absorption of light in high temperature biological tissue embedded with O-PCNPs under laser irradiation with carefully selected laser wavelengths, O-PCMs, and nanoparticle sizes or shapes.

Fig. 2 Absorption efficiency of a-state and c-state VO_2 nanosphere with radius (a) r = 30 nm; (b) r = 60 nm; (c) r = 90 nm; (d) r = 120 nm.

Fig. 3 Absorption efficiency of a-state and c-state GST nanosphere with radius (a) r = 30 nm; (b) r = 60 nm; (c) r = 90 nm; (d) r = 120 nm.

Fig. 4 Optical properties of (a) VO_2 and (b) GST nanospheres with R = 90 nm at amorphous and crystalline states.

It should be noted that since the melting point of VO_2 is much higher than the optical phase change temperature, nanoparticles will not degrade or submit to reshaping effect during the process of photothermal therapy. Also, since the optical phase change process is reversible, the nanoparticles are functional for multiple therapeutic circles.

When considering nanoparticles' application in laser induced thermal therapy, the biocompatibility and toxicity should also be considered. The toxicity of VO_2 nanoparticles has been investigated for some bacterial strains [59]. It was found that only extremely high concentration (above 200 μg/mL) of VO_2 nanoparticles can lead to a noticeable decrease of cell concentration. However, the concentration needed to produce an increase of temperature in tissue is much lower than that (about 0.2 μg/mL in the present work). Therefore, the toxicity of VO_2 nanoparticles should be acceptable. However, it still needs further investigation in biological systems. In addition, this situation can be further improved by modifying the nanoparticles with SiO_2 or other materials. Therefore, the optical properties of abovementioned nanosphere modified with SiO_2 shell are investigated. It is found that the trends of spectral absorption efficiency for SiO_2@VO_2 and SiO_2@GST nanoshells are pretty similar with those of the VO_2 and GST nanospheres, with a slight increase of the absolute value of the absorption efficiency (see Fig. 5). It should be noted that in the present work, the absorption efficiency of nanoshell is obtained by calculating the ratio of absorption cross section and the physical cross section of the core sphere. The results are consistent with those of our previous work [60]. When the refractive index of the coating material (~1.5) is larger than that of the matrix media (1.33), the absorption efficiency of

the nanoparticle could be enhanced. Meanwhile, the wavelength-dependent *P* value are almost the same for different SiO_2 shell thickness (see Fig. 6), which means the SiO_2 shell has the same influence on the nanoparticles before and after phase change.

Fig. 5 Optical properties of VO_2 (a-c) and GST (d-f) nanoshells at amorphous and crystalline states with shell thickness: (a) 5 nm; (b) 10 nm; (c) 20 nm; (d) 5 nm; (e) 10 nm; (f) 20 nm.

Fig. 6 Figure of merit *P* as a function of wavelength for different shell thickness t_{sh}.

3.2 Light transfer in nanoparticle embedded biological tissue

A bioheat transfer model is used to show the advantage of optical phase change nanomaterials assisted photothermal therapy. The geometrical model and boundary conditions are illustrated in Fig. 7a. The boundary conditions are very important for the prediction of temperature distribution in biological tissue [52]. For the sake of simplicity, the Dirichlet boundary conditions are applied for the surrounding walls. The optical properties of normal and cancerous tissue are set as the same as those of human dermis and skin cancer (nodular basal cell carcinoma) at 630 nm (see Table 1). The SiO_2@VO_2 nanoshell with core radius R = 90 nm and shell thickness t_{sh} = 5 nm is applied. Before phase change (amorphous state), the absorption and scattering efficiencies of the nanoshell are 1.355 and 1.889, respectively, which after phase change (crystalline state) are 1.066 and 0.853, respectively. The optical properties of the nanoparticle embedded tissue can be calculated using Eq. 11. The absorption and scattering coefficients of nanoparticle systems, $\mu_{a,n}$ and $\mu_{s,n}$, can be expressed as [61]:

$$\mu_{a,n} = 0.75 f_v \frac{Q_{abs}}{r} \tag{17}$$

$$\mu_{s,n} = 0.75 f_v \frac{Q_{sca}}{r} \tag{18}$$

where f_v is the volume fraction of nanoparticles. If the volume fraction of nanoparticles in cancerous tissue is $f_v = 4.5 \times 10^{-5}$, the nanoparticle induced absorption and scattering coefficients can be calculated by Eqs. 17 and 18, which are 0.508 mm^{-1} and 0.708 mm^{-1} (before phase change), 0.400 mm^{-1} and 0.320 mm^{-1} (after phase change), respectively. It should be noted that the volume fraction of nanoparticles has significant influence on the process of photothermal therapy. Details can be found in our previous work, which will not be introduced here [1, 62].

Table 1 Optical properties of normal and cancerous tissue in 630 nm [63]

The scattering directivity of nanoparticles strongly affects the light transfer in biological tissue during photothermal therapy. Therefore, the radiation patterns of the abovementioned nanoshells are calculated (see Fig. 7b). It can be seen that before and after phase change, the SiO_2@VO_2 nanoshells are predominately scattered to the forward direction, which is helpful to improve the penetration depth of light. The scattering phase function of nanoparticle system are fitted as asymmetry factor g in Heney-Greenstein (H-G) phase function [64], which for a-state and c-state nanoparticles are 0.3459 and 0.3151, respectively (see Fig. 8). Fig 7c shows the SAR distributions of the abovementioned model. It is obvious that when the nanoparticles in tumor change from a-state to c-state, the SAR distribution in the tumorous area will be relatively more uniform. More importantly, light energy absorbed around the upper interface between tumor and healthy tissue is reduced significantly (black arrows).

Fig. 7 SAR distribution in tumor. (a) Geometric model and boundary conditions for light and heat transfer during photothermal therapy; (b) radiation patterns of a-state and c-state VO_2 nanospheres with radius R = 90 nm. FWD and BWD mean forward and backward directions, respectively; (c) SAR distributions in tumorous area embedded with a-state and c-state nanospheres.

Fig. 8 Fitted results of H-G function and the radiation pattern of a-state and c-state VO_2 nanospheres with radius R = 90 nm.

In the abovementioned cases, the nanoparticles in the whole tumor are assumed to be fully changed from amorphous state to crystalline state. However, in the actual process, this transition is taken place gradually from the top to the bottom of the tumor accompanying with the expansion of high temperature zone (above phase transition temperature). Inside the high temperature zone, the embedded nanoparticles are in crystalline state, while in other parts of the tumor, the nanoparticles are in amorphous state. Fig. 9 shows the SAR distributions for different sizes of high temperature zone which are circled by dotted lines. The high temperature zone is defined as the intersection of the tumor and a hypothetical circle which has the same size of the tumor right above the tumor. Therefore, the expansion of the high temperature zone can be simulated as the moving downwards of the hypothetical circle. From Fig. 9 it can be seen that in the upper boundary of the high temperature zone (black arrows), the light energy absorbed by the tumor is reduced significantly, which is similar to the former case (see Fig. 7c). More importantly, due to the decrease of the absorption coefficient in the phase transition area, the energy attenuation is also

reduced. Therefore, a light absorption peak is generated in the lower boundary of the high temperature zone (red arrows).

Fig. 9 SAR distributions for different sizes of high temperature zone. The high temperature zone is loaded with c-state nanoparticles and the rest part of the tumor is loaded with a-state nanoparticles.

The SAR distributions along the center line of the model for different size of high temperature zone is illustrated in Fig. 10. $z = 0$ means phase transition of nanoparticles is not considered. $z = 1$, 2, and 3 mm means the hypothetical high temperature circle moving downward for 1, 2, and 3 mm, respectively. It can be seen clearly that an absorption peak between the high and low temperature zone will generate if the high temperature zone is loaded with c-state nanoparticle and low temperature zone is loaded with a-state nanoparticles. This absorption peak will shift with the expansion of the high temperature zone, and will contribute to improve the temperature increase rate in the low temperature area. As a result, the overall temperature distribution will be more uniform compared to the situation without considering the phase change of nanoparticles.

Fig. 10 SAR distributions along the center line of the model for different sizes of high temperature zone. z = 1, 2, and 3 mm means the hypothetical high temperature circle moving downward for 1, 2, and 3 mm, respectively.

As mentioned above, the absorption efficiency of SiO_2@VO_2 nanoshell with core radius R = 90 nm and shell thickness t_{sh} = 5 nm before and after phase change are 1.355 and 1.066,

respectively, which means *P* equals to 0.21. It is possible that the value of *P* can be further reduced with the development of new O-PCMs or better types of nanoparticle (sizes, shapes, structures, or components). Therefore, we further studied the influence of *P* on the SAR distributions. Fig. 11 shows the SAR distributions for different *P* (0.21, 0.3, 0.5, and 0.8), which is realized by changing the absorption cross section of c-state nanoparticles and keeping other parameters the same. It can be seen that with the increasing of *P*, the light energy absorbed in the upper boundary of high temperature zone is further reduced. Meanwhile, the light absorbed in the lower boundary of the high temperature zone is enhanced, which is due to the fact that the light attenuation is reduced along the light path.

Fig. 11 SAR distribution for different absorption cross section of c-state nanoparticles: (a-d) *z* = 1 mm; (e-h) *z* = 1.5 mm.

3.3 Light transfer in other typical tissues

In the above analysis, the optical properties of the normal tissue and tumor are based on the measured results of human dermis and skin cancer with the characteristics of strong scattering. In this section, two other typical tumors, breast tumor and prostate tumor, are investigated based on the same model. Compared to the human dermis, the breast tumor is relatively weaker in scattering and the prostate tumor is both weak in scattering and absorbing. The optical properties used are listed in Table 2. The properties of nanoparticles are set the same as last section. It should be noted that the reduced scattering coefficients μ_s' ($=\mu_s(1-g)$) are given instead of scattering coefficients μ_s. For scattering dominated media, i.e., $\mu_s'/(\mu_a+\mu_s')>0.5$, if the reduced scattering coefficients are the same, then identical light transfer phenomenon can be obtained even their scattering

coefficients and asymmetry factors are not the same [65]. In another word, forward scattering can be approximated by using reduced absorption and scattering coefficients along with a phase function set to 1, and vice versa. Therefore, in the following cases, the asymmetry factors of normal and cancerous tissues are assumed to be g = 0.8. Then the reduced absorption and scattering coefficients are replaced by $\mu_s = \mu_s' / (1-g)$.

Figs. 12 and 13 illustrate the SAR distributions of breast tumor and prostate tumor under laser irradiation. Similar to the results of skin cancer, a reduction of light absorbed in the upper surface of tumor and an increase of light absorbed in the lower boundary of the tumor are observed for each case. Moreover, the specific absorption rate is reduced dramatically in the high temperature zone and increased correspondingly in the low temperature zone with the increasing of *P* (see Fig. 14). It can be concluded that the proposed method is valid for different types of tumors with different optical properties.

Table 2 Optical properties of breast and prostate tissues [66-68]

Fig. 12 SAR distributions for different sizes of high temperature zone for breast tumor.

Fig. 13 SAR distributions for different sizes of high temperature zone for prostate tumor.

Fig. 14 SAR distributions along the center line of the model for different values of *P*.

3.4 Transient thermal response of biological tissue embedded with O-PCNPs

The thermal response of the laser irradiated biological tissue embedded with O-PCNPs are investigated in this section. The thermal properties are listed in Table 3. The optical properties are set the same as those of the prostate tumor. It should be noted that under laser irradiation, the temperature of the nanoparticle is not equal to the bulk temperature of the biological tissue matrix. The temperature difference may be ranging from several Kelvins to 250 K or higher [69, 70], which is depending on many factors, such as the particle concentration and laser power density, which needs further investigation and within the scope of this work. Therefore, considering the optical phase change temperature of VO_2 is about 68 ℃, in the following cases, the bulk temperature of the tissue that can induce the phase change of the embedded nanoparticles is set as 40 ℃. Meanwhile, the influence of the bulk temperature of tissue matrix that will induce the phase transition of nanoparticles is also investigated.

Table 3 Thermal properties of prostate and tumor [56]

Fig. 15 shows the temperature change of two points (shown in the inset of Fig. 15b) with and without considering the phase change of the embedded nanoparticles. It can be seen clearly that the temperature difference between points A and B drops dramatically if the phase transition of nanoparticles is considered, which is owing to the reduction of absorption coefficient along the light path. When the temperature of a certain location reaches 40 ℃ (phase transition temperature), the absorption cross section of nanoparticles embedded in this location will suddenly drop, which leads to a reduction of the local heat generation rate and temperature increasing rate. Naturally, the light energy transferred to deeper tissue will increase. Therefore, the heat generation rate and temperature increasing rate of deeper tissue will also increase (Fig. 15b). As a result, the temperature distribution in the tumor will be much more uniform compared to the cases without

considering the phase change of nanoparticles. Fig. 16 illustrates the temperature distribution along the center line of the model. Although the overall temperature level is reduced after considering the phase change of nanoparticles, the temperature uniformity is increased in the tumorous area. Therefore, the proposed strategy of using phase change nanomaterials to improve the temperature uniformity in tumor during laser induced thermal therapy is proved to be valid.

Fig. 15 Temperature profiles of two points inside tumor with and without considering phase change of embedded nanoparticles. Laser power density is set as 2.0 x 10^4 W/m^2.

Fig. 16 Temperature distribution along the center line of the model at different time: (a) *t* = 20 s, (b) *t* = 40 s, (c) *t* = 60 s, (d) *t* = 80 s. The red solid lines are the temperature profile without considering the optical phase change of nanoparticles and the black dashed lines are the temperature profiles considering the optical phase change of nanoparticles.

As mentioned, the nanoscale temperature of nanoparticles is not the same with the bulk temperature of biological tissue. Therefore, in this work, the influence of the phase change temperature (bulk temperature of tissue) is investigated (Fig. 17). It is assumed that when the temperature of the tissue matrix reaches 40, 45, or 50 ℃, the phase of the embedded nanoparticles will change from amorphous state to crystalline state. It should be noted that this temperature can be tuned by adjusting the laser power and time of exposure. It can be seen from Fig. 17 that the phase transition temperature has a great influence on the temperature uniformity in the early stage of laser heating. However, in the later stage, the temperature difference between point A and B is almost the same for different phase transition temperature. The reason is that after the temperature

of the matrix tissue is higher than the phase transition temperature, the SAR distribution is not relevant to the phase transition temperature since the embedded nanoparticles are all turned into crystalline state.

Fig. 17 Temperature difference between point A and B for different temperature of tissue which can induce the phase transition of nanoparticles.

To illustrate the performance of the proposed temperature control method more clearly, the 2D temperature distribution with and without considering the phase change of nanoparticles are shown in Figs. 18 and 19. It is obvious that compared to not considering phase change ($P = 0$), the high temperature zone is larger inside the tumor, which means the temperature distribution is more uniform inside tumor. Moreover, the high temperature zone is more likely to be confined inside the tumor for larger value of P (blue arrows). In conclusion, the proposed passive control method can be applied to improve the temperature uniformity in cancerous tissue during LITT and advanced O-PCMs or new types of nanoparticles should be further investigated to improve the performance (identified by figure of merit P) of the proposed method. It should be noted that the optical phase change nanoparticles do not undergo sharp transition from amorphous to crystalline state. However, this process should be completed in a few Kelvins. Therefore, the optical properties needed to achieve the passive temperature control during photothermal therapy will still be satisfied, only with a small reduction of the figure of merit P.

Fig. 18 Temperature distributions at 20 s for different values of P when the phase transition temperature is set as 40℃: (a) $P = 0$; (b) $P = 0.21$; (c) $P = 0.8$.

Fig. 19 Temperature distributions at 100 s for different values of *P* when the phase transition temperature is set as 40℃: (a) *P* = 0; (b) *P* = 0.21; (c) *P* = 0.8.

4. Conclusions

In the present work, we proposed a method that can be used to improve the uniformity of temperature distribution inside tumorous tissue during LITT. Optical phase change nanomaterials are utilized to replace the commonly used noble metal nanoparticles to enhance and adjust the localized light absorption in tumor. It was found that, when the radius of phase change nanosphere is larger than 90 nm, the absorption cross sections of crystalline state VO_2 and GST nanospheres will be smaller than those of their amorphous state counterparts in a certain waveband. A figure of merit *P* is proposed to describe the difference of absorption cross section of nanoparticles in a-state and c-state quantificationally. When the phase change nanospheres are adopted as thermal contrast agents, results show that in the early stage of LITT, the O-PCNPs can be used to improve the specific absorption rate in the targeted region, similar to noble metal nanoparticles. However, after the local temperature reaches the phase transition temperature, the O-PCNPs convert from amorphous state to crystalline state, which leads to the decrease of temperature increasing rate in corresponding area. Therefore, in the high temperature zone the local temperature increasing rate reduces owing to the reduction of local heat generation rate. On the contrary, the temperature increasing rate improves in the low temperature zone since more energy is transferred to the deeper tissue, which results in a more uniform temperature distribution in tumorous region. On this basis, the influence of phase transition temperature and value of *P* on the performance of the proposed nanoagents is investigated. Results show that phase transition temperature only has an influence

on the temperature profiles in the early stage of laser heating. Meanwhile, the value of *P* is a very important parameter indicating the possible potential of the O-PCNPs to be used in LITT. Larger value of *P* will lead to a more uniform temperature distribution in tumor and the overheating area is more likely to be constrained inside tumor. Moreover, the performance of the proposed method can be further improved by tuning the size and shape of the O-PCNPs. Further investigation will focus on the experimental validation of the proposed method and the development of other nanoagents with larger value of *P*.

Conflict of Interest

The authors declare no competing financial interest.

Acknowledgment

This project has received funding from the National Natural Science Foundation of China (51806047), China Postdoctoral Science Foundation (2019T120264), Natural Science Foundation of Heilongjiang Province (LH2019E047), and the European Union's Horizon 2020 research and innovation programme under the Marie Skłodowska-Curie grant agreement No. 839641.

References

[1] Ren Y., Qi H., Chen Q., Ruan L., Thermal dosage investigation for optimal temperature distribution in gold nanoparticle enhanced photothermal therapy, Int. J. Heat Mass Tran., 106 (2017) 212-221.

[2] Choi C.K.K., Chiu Y.T.E., Zhuo X., Liu Y., Pak C.Y., Liu X., Tse Y.S., Wang J., Choi C.H.J., Dopamine-Mediated Assembly of Citrate-Capped Plasmonic Nanoparticles into Stable Core-Shell Nanoworms for Intracellular Applications, ACS Nano, 13 (2019) 5864-5884.

[3] Tao C., An L., Lin J., Tian Q., Yang S., Surface Plasmon Resonance–Enhanced Photoacoustic Imaging and Photothermal Therapy of Endogenous H2S-Triggered Au@Cu2O, Small, 15 (2019) 1903473.

[4] Simón M N.K., Jørgensen JT, Oddershede LB, Kjaer A, Fractionated photothermal therapy in a murine tumor model: comparison with single dose, Int. J. Nanomed., 14 (2019) 5369-5379.

[5] Rubio-Ruiz B., Perez-Lopez A.M., Bray T.L., Lee M., Serrels A., Prieto M., Arruebo M., Carragher N.O., Sebastian V., Unciti-Broceta A., High-Precision Photothermal Ablation Using Biocompatible Palladium Nanoparticles and Laser Scanning Microscopy, ACS Appl Mater Interfaces, 10 (2018) 3341-3348.

[6] Fu R., Yan Y., Roberts C., Liu Z., Chen Y., The role of dipole interactions in hyperthermia heating colloidal clusters of densely-packed superparamagnetic nanoparticles, Sci. Rep-UK, 8 (2018) 4704.

[7] Kumar D., Singh S., Sharma N., Rai K.N., Verified non-linear DPL model with experimental data for analyzing heat transfer in tissue during thermal therapy, Int. J. Therm. Sci., 133 (2018) 320-329.

[8] Huang X., Jain P.K., El-Sayed I.H., El-Sayed M.A., Plasmonic photothermal therapy (PPTT) using gold nanoparticles, Laser Med. Sci., 23 (2008) 217-228.

[9] Yu L., Jian X., Dong F., Cui Y., Dual-wavelengths photoacoustic temperature measurement, in, 2017.

[10] Lin K.H., Young S.Y., Hsu M.C., Chan H., Focused ultrasound thermal therapy system with ultrasound image guidance and temperature measurement feedback, in: International Conference of the IEEE Engineering in Medicine & Biology Society, IEEE, 2008.

[11] Tarapacki C., Kumaradas C., Karshafian R., Enhancing laser thermal-therapy using ultrasound-microbubbles and gold nanorods of in vitro cells, Ultrasonics, 53 (2013) 793-798.
[12] Zhang T., Jiang Z., Xve T., Sun S., Li J., Ren W., Wu A., Huang P., One-pot synthesis of hollow PDA@DOX nanoparticles for ultrasound imaging and chemo-thermal therapy in breast cancer, Nanoscale, 11 (2019).
[13] Chen B.T., Shieh J., Huang C.-W., Chen W.-S., Chen S.-R., Chen C.-S., Ultrasound Thermal Mapping Based on a Hybrid Method Combining Physical and Statistical Models, Ultrasound Med. Biol., 40 (2014) 115-129.
[14] Huang S.M., Liu H.L., Li M.L., Improved temperature imaging of focused ultrasound thermal therapy using a sigmoid model based cross-correlation algorithm, in: 2012 International Ultrasonics Symposium, 2012.
[15] Zhou Y., Tang E., Luo J., Yao J., Deep-tissue temperature mapping by multi-illumination photoacoustic tomography aided by a diffusion optical model: A numerical study, J. Biomed. Opt., 23 (2018) 1.
[16] Kinsey A.M., Diederich C.J., Nau W.H., Rieke V., Butts R.K., Sectored interstitial ultrasound applicators for angular control of MR-guided thermal therapy, Proc Spie, 5698 (2005) 1352-1363.
[17] Senneville B.D.D., Quesson B., Moonen C.T.W., Magnetic Resonance Temperature Imaging, International journal of hyperthermia : the official journal of European Society for Hyperthermic Oncology, North American Hyperthermia Group, 21 (2005) 515-532.
[18] Stafford R.J., Shetty A., Elliott A.M., Klumpp S.A., McNichols R.J., Gowda A., Hazle J.D., Ward J.F., Magnetic Resonance Guided, Focal Laser Induced Interstitial Thermal Therapy in a Canine Prostate Model, Journal of Urology, 184 (2010) 1514-1520.

[19] Zhu X., Feng W., Chang J., Tan Y.W., Li J., Chen M., Sun Y., Li F., Temperature-feedback upconversion nanocomposite for accurate photothermal therapy at facile temperature, Nat. Commun., 7 (2016) 10437.

[20] Soni S., Tyagi H., Taylor R.A., Kumar A., Investigation on nanoparticle distribution for thermal ablation of a tumour subjected to nanoparticle assisted thermal therapy, J. Therm. Biol., 43 (2014) 70-80.

[21] Soni S., Tyagi H., Taylor R.A., Kumar A., Role of optical coefficients and healthy tissue-sparing characteristics in gold nanorod-assisted thermal therapy, Int. J. Hyperther., 29 (2013) 87-97.

[22] Chen G., Stang J., Haynes M., Leuthardt E., Moghaddam M., Real-Time Three-Dimensional Microwave Monitoring of Interstitial Thermal Therapy, IEEE Trans. Biomed. Eng., 65 (2018) 528-538.

[23] Gupta P.K., Singh J., Rai K.N., Numerical simulation for heat transfer in tissues during thermal therapy, J. Therm. Biol., 35 (2010) 295-301.

[24] Shih T.C., Kou H.S., Liauh C.T., Lin W.L., The impact of thermal wave characteristics on thermal dose distribution during thermal therapy: A numerical study, Med. Phys., 32 (2005) 3029-3036.

[25] Mesicek J., Kuca K., Summary of numerical analyses for therapeutic uses of laser-activated gold nanoparticles, Int. J. Hyperther., 34 (2018) 1-35.

[26] Fuentes D., Walker C., Elliott A., Shetty A., Stafford R.J., Magnetic resonance temperature imaging validation of a bioheat transfer model for laserinduced thermal therapy, International journal of hyperthermia : the official journal of European Society for Hyperthermic Oncology, North American Hyperthermia Group, 27 (2011) 453-464.

[27] Kumar D., Rai K.N., Numerical simulation of time fractional dual-phase-lag model of heat transfer within skin tissue during thermal therapy, J. Therm. Biol., 67 (2017) 49-58.

[28] Kumar P., Kumar D., Rai K.N., Numerical simulation of dual-phase-lag bioheat transfer model during thermal therapy, Math. Biosci., 281 (2016) 82-91.

[29] Patidar S., Kumar S., Srivastava A., Singh S., Dual phase lag model-based thermal analysis of tissue phantoms using lattice Boltzmann method, Int. J. Therm. Sci., 103 (2016) 41-56.

[30] Yuan P., Yang C.-S., Liu S.-F., Temperature analysis of a biological tissue during hyperthermia therapy in the thermal non-equilibrium porous model, Int. J. Therm. Sci., 78 (2014) 124-131.

[31] Sadia S., S.B. N., Naheed B., S.E. A., M.A. H., Thermal radiation therapy of biomagnetic fluid flow in the presence of localized magnetic field, Int. J. Therm. Sci., (2018).

[32] Zhang Y., Li J., Chou J.B., Fang Z., Yadav A., Lin H., Du Q., Michon J., Han Z., Huang Y., Zheng H., Gu T., Liberman V., Richardson K., Hu J., Broadband Transparent Optical Phase Change Materials, in: Lasers and Electro-Optics, OSA Technical Digest, Optical Society of America, 2017.

[33] Wu S.R., Lai K.-L., Wang C.-M., Passive temperature control based on a phase change metasurface, Sci. Rep-UK, 8 (2018) 7684.

[34] Sarangan A., Duran J., Vasilyev V., Limberopoulos N., Vitebskiy I., Anisimov I., Broadband Reflective Optical Limiter Using GST Phase Change Material, IEEE Photonics Journal, 10 (2018) 1-9.

[35] Zhang Y., Chou J.B., Li J., Li H., Du Q., Yadav A., Zhou S., Shalaginov M.Y., Fang Z., Zhong H., Roberts C., Robinson P., Bohlin B., Ríos C., Lin H., Kang M., Gu T., Warner J.,

Liberman V., Richardson K., Hu J., Broadband Transparent Optical Phase Change Materials for High-Performance Nonvolatile Photonics, Nat. Commun., 10 (2019) 1-9.

[36] Weifeng, Jiang, Nonvolatile and ultra-low-loss reconfigurable mode (De)multiplexer/switch using triple-waveguide coupler with Ge2Sb2Se4Te1 phase change material, Sci. Rep-UK, 8 (2018) 15946.

[37] Bucharskaya A.B., N. M.G., L. C.M., S. T.G., A. N.N., N. K.B., G. K.N., N. B.A., A. G.E., V. T.V., Plasmonic photothermal therapy: Approaches to advanced strategy, Lasers in Surgery & Medicine, (2018).

[38] Huang X., El-Sayed M.A., Plasmonic photo-thermal therapy (PPTT), Alex. J. Med., 47 (2011) 1-9.

[39] Malvindi M.A., Brunetti V., Vecchio G., Galeone A., Pompa P.P., SiO2 nanoparticles biocompatibility and their potential for gene delivery and silencing, Nanoscale, 4 (2011) 486-495.

[40] Malvindi M.A., Matteis V.D., Galeone A., Brunetti V., Anyfantis G.C., Athanassiou A., Cingolani R., Pompa P.P., Toxicity Assessment of Silica Coated Iron Oxide Nanoparticles and Biocompatibility Improvement by Surface Engineering, Plos One, 9 (2014).

[41] Cha J., Cui P., Lee J.-K., A simple method to synthesize multifunctional silica nanocomposites, NPs@SiO2, using polyvinylpyrrolidone (PVP) as a mediator, Journal of Materials Chemistry, 20 (2010) 5533-5537.

[42] Gschwend P.M., Krumeich F., Pratsinis S.E., 110th Anniversary: Synthesis of Plasmonic Silica-Coated TiN Particles, Industrial & Engineering Chemistry Research, 58 (2019).

[43] Draine B.T., Flatau P.J., Discrete-dipole approximation for scattering calculations, J. Opt. Soc. Am. A, 11 (1994) 1491-1499.

[44] Draine B.T., Discrete-dipole approximation and its application to interstellar graphite grains, Astrophys. J., 333 (1988) 848-872.

[45] Gang X., Yong C., Masato T., Ping J., Surface plasmon resonance of silver nanoparticles on vanadium dioxide, J. Phys. Chem. B, 110 (2006) 2051-2056.

[46] Michel A.K., Chigrin D.N., Maß T.W., Schönauer K., Salinga M., Wuttig M., Taubner T., Using low-loss phase-change materials for mid-infrared antenna resonance tuning, Nano Lett., 13 (2013) 3470.

[47] Ren Y., Qi H., Chen Q., Wang S., Ruan L., Localized surface plasmon resonance of nanotriangle dimers at different relative positions, J. Quant. Spectrosc. Ra., 199 (2017) 45-51.

[48] Pennes H.H., Analysis of tissue and arterial blood temperatures in the resting human forearm, J. Appl. Physiol., 1 (1948) 93-122.

[49] Asllanaj F., Contassot-Vivier S., Liemert A., Kienle A., Radiative transfer equation for predicting light propagation in biological media: comparison of a modified finite volume method, the Monte Carlo technique, and an exact analytical solution, J. Biomed. Opt., 19 (2014) 015002.

[50] Nirgudkar H., Kumar S., Srivastava A., Solution of Radiative Transfer Equation using Discrete Transfer Method for two-dimensional participating medium, International Communications in Heat & Mass Transfer, 61 (2015) 88-95.

[51] Dombrovsky L.A., Timchenko V., Jackson M., Indirect heating strategy for laser induced hyperthermia: An advanced thermal model, Int. J. Heat Mass Tran., 55 (2012) 4688-4700.

[52] Kumar S., Srivastava A., Finite integral transform-based analytical solutions of dual phase lag bio-heat transfer equation, Appl. Math. Model., 52 (2017) 378-403.

[53] Phadnis A., Kumar S., Srivastava A., Numerical investigation of thermal response of a laser-irradiated biological tissue phantoms embedded with gold nanoshells, J. Therm. Biol., 61 (2016) 16-28.

[54] Deka B., Dutta J., Finite element methods for non-fourier thermal wave model of bio heat transfer with an interface, J. Appl. Math. Comput., 62 (2020) 701-724.

[55] Ahmadikia H., Moradi A., Fazlali R., Parsa A.B., Analytical solution of non-Fourier and Fourier bioheat transfer analysis during laser irradiation of skin tissue, J. Mech. Sci. Technol., 26 (2012) 1937-1947.

[56] Manuchehrabadi N., Zhu L., Development of a computational simulation tool to design a protocol for treating prostate tumours using transurethral laser photothermal therapy, Int. J. Hyperther., 30 (2014) 349-361.

[57] Manuchehrabadi N., Chen Y., Lebrun A., Ma R., Zhu L., Computational simulation of temperature elevations in tumors using Monte Carlo method and comparison to experimental measurements in laser photothermal therapy, Journal of biomechanical engineering, 135 (2013) 121007.

[58] Prahl S.A., Keijzer M., Jacques S.L., Welch A.J., A Monte Carlo model of light propagation in tissue, in: SPIE Proceedings of Dosimetry of Laser Radiation in Medicine and Biology, 1989, pp. 102-111.

[59] Wu D., Su Q., Li Y., Zhang C., Qin X., Liu Y.Y., Xi W.S., Gao Y., Cao A., Liu X., Toxicity assessment and mechanistic investigation of engineered monoclinic VO2 nanoparticles, Nanoscale, 10 (2018).

[60] Chen Q., Ren Y., Qi H., Ruan L., Influence of PEG coating on optical and thermal response of gold nanoshperes and nanorods, J. Quant. Spectrosc. Ra., (2018).

[61] Dombrovsky L.A., Timchenko V., Jackson M., Yeoh G.H., A combined transient thermal model for laser hyperthermia of tumors with embedded gold nanoshells, Int. J. Heat Mass Tran., 54 (2011) 5459-5469.

[62] Yin Y., Ren Y., Li H., Qi H., Characteristic analysis of light and heat transfer in photothermal therapy using multiple-light-source heating strategy, Int. J. Therm. Sci., 158 (2020) 106533.

[63] Karsten A.E., Singh A., Effect of skin tumor properties on laser penetration, in: European Conferences on Biomedical Optics, 2009.

[64] Qi H., Ren Y.T., Chen Q., Ruan L.-M., Fast method of retrieving the asymmetry factor and scattering albedo from the maximum time-resolved reflectance of participating media, Appl. Opt., 54 (2015) 5234-5242.

[65] Welch A.J., van Gemert M.J.C., Optical-Thermal Response of Laser-Irradiated Tissue, Springer, 2011.

[66] Yang Z., Yuan Y., Tuchin V.V., Chen Y., Xiang W., Liu C., Jing W., Xue X., Dan Z., VIS-NIR spectrum analysis for distinguishing tumor and normal human breast tissue, in: Dynamics and Fluctuations in Biomedical Photonics IX, San Francisco, 2012.

[67] Svensson T., Andersson-Engels S., Einarsdottir M., Svanberg K., In vivo optical characterization of human prostate tissue using near-infrared time-resolved spectroscopy, J. Biomed. Opt., 12 (2007) 014022.

[68] Cheong W.F., Prahl S.A., Welch A.J., A review of the optical properties of biological tissues, IEEE Journal of Quantum Electronics, 26 (1990) 2166-2185.

[69] Kang P., Chen Z., Nielsen S.O., Hoyt K., D"Arcy S., Gassensmith J.J., Qin Z., Thermoplasmonics: Molecular Hyperthermia: Spatiotemporal Protein Unfolding and Inactivation by Nanosecond Plasmonic Heating (Small 36/2017), Small, 13 (2017) 1700841.

[70] Baffou G., Berto P., Bermúdez Ureña E., Quidant R., Monneret S., Polleux J., Rigneault H., Photoinduced heating of nanoparticle arrays, ACS Nano, 7 (2013) 6478-6488.

Table Captions

Table 1 Optical properties of normal and cancerous tissue in 630 nm [63]

Table 2 Optical properties of breast and prostate tissues [66-68]

Table 3 Thermal properties of prostate and tumor [56]

Table 1 Optical properties of normal and cancerous tissue in 630 nm [63]

Types	asymmetry factor g	Absorption coefficient μ_a (mm^{-1})	Absorption coefficient μ_s (mm^{-1})
Dermis	0.82	0.16	16.94
Nodular basal cell carcinoma	0.8	0.13	11.5

Table 2 Optical properties of breast and prostate tissues [66-68]

Parameters	Absorption efficiency mm^{-1}	Reduced scattering efficiency mm^{-1}
Normal breast tissue	0.138	1.553
Breast tumor	0.101	1.967
Normal prostate tissue	0.05	0.87
Prostate tumor	0.039	0.337

Table 3 Thermal properties of prostate and tumor [56]

Parameters	Thermal conductivity $Wm^{-1}K^{-1}$	Heat capacity $JKg^{-1}K^{-1}$	Density Kgm^{-3}	Metabolic heat generation rate Q_{met} Wm^{-3}	Blood perfusion s^{-1}	Blood temperature °C
Prostate	0.5	3780.0	1060.0	15333.0	—	—
Tumor	0.5	3780.0	1060.0	2083.0	—	—
Blood	—	4200.0	1000.0	—	0.00613	36.5

Figure Captions

Fig. 1 Flowchart of Monte Carlo method.

Fig. 2 Absorption efficiency of a-state and c-state VO_2 nanosphere with radius (a) r = 30 nm; (b) r = 60 nm; (c) r = 90 nm; (d) r = 120 nm.

Fig. 3 Absorption efficiency of a-state and c-state GST nanosphere with radius (a) r = 30 nm; (b) r = 60 nm; (c) r = 90 nm; (d) r = 120 nm.

Fig. 4 Optical properties of (a) VO_2 and (b) GST nanospheres with R = 90 nm at amorphous and crystalline states.

Fig. 5 Optical properties of VO_2 (a-c) and GST (d-f) nanoshells at amorphous and crystalline states with shell thickness: (a) 5 nm; (b) 10 nm; (c) 20 nm; (d) 5 nm; (e) 10 nm; (f) 20 nm.

Fig. 6 Figure of merit P as a function of wavelength for different shell thickness t_{sh}.

Fig. 7 SAR distribution in tumor. (a) Geometric model and boundary conditions for light and heat transfer during photothermal therapy; (b) radiation patterns of a-state and c-state VO_2 nanospheres with radius R = 90 nm. FWD and BWD mean forward and backward directions, respectively; (c) SAR distributions in tumorous area embedded with a-state and c-state nanospheres.

Fig. 8 Fitted results of H-G function and the radiation pattern of a-state and c-state VO_2 nanospheres with radius R = 90 nm.

Fig. 9 SAR distributions for different sizes of high temperature zone. The high temperature zone is loaded with c-state nanoparticles and the rest part of the tumor is loaded with a-state nanoparticles.

Fig. 10 SAR distributions along the center line of the model for different sizes of high temperature zone. z = 1, 2, and 3 mm means the hypothetical high temperature circle moving downward for 1, 2, and 3 mm, respectively.

Fig. 11 SAR distribution for different absorption cross section of c-state nanoparticles: (a-d) z = 1 mm; (e-h) z = 1.5 mm.

Fig. 12 SAR distributions for different sizes of high temperature zone for breast tumor.

Fig. 13 SAR distributions for different sizes of high temperature zone for prostate tumor.

Fig. 14 SAR distributions along the center line of the model for different values of P.

Fig. 15 Temperature profiles of two points inside tumor with and without considering phase change of embedded nanoparticles. Laser power density is set as 2.0×10^4 W/m^2.

Fig. 16 Temperature distribution along the center line of the model at different time: (a) t = 20 s, (b) t = 40 s, (c) t = 60 s, (d) t = 80 s. The red solid lines are the temperature profile without considering the optical phase change of nanoparticles and the black dashed lines are the temperature profiles considering the optical phase change of nanoparticles.

Fig. 17 Temperature difference between point A and B for different temperature of tissue which can induce the phase transition of nanoparticles.

Fig. 18 Temperature distributions at 20 s for different values of P when the phase transition temperature is set as 40℃: (a) P = 0; (b) P = 0.21; (c) P = 0.8.

Fig. 19 Temperature distributions at 100 s for different values of P when the phase transition temperature is set as 40℃: (a) P = 0; (b) P = 0.21; (c) P = 0.8.

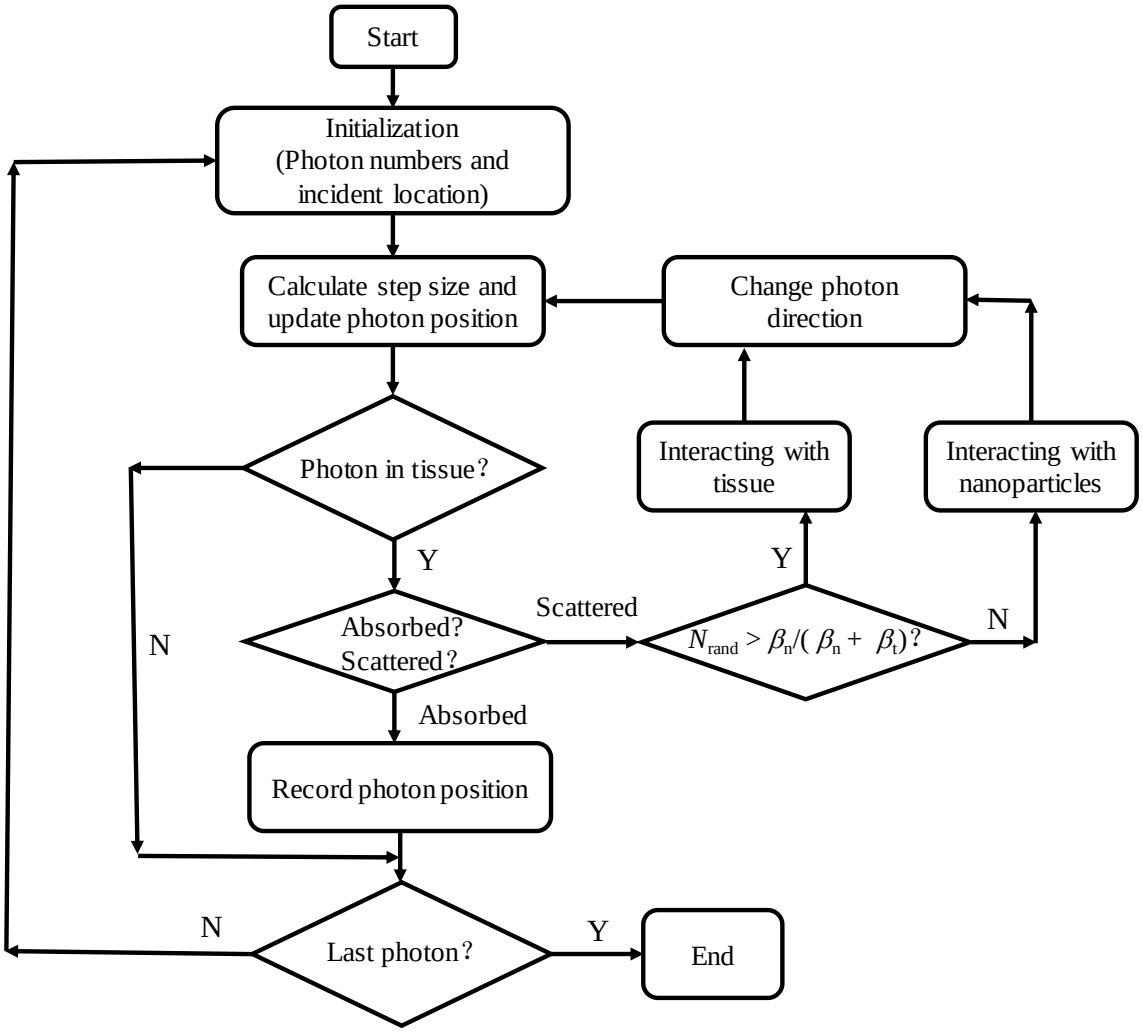

Fig. 1 Flowchart of Monte Carlo method.

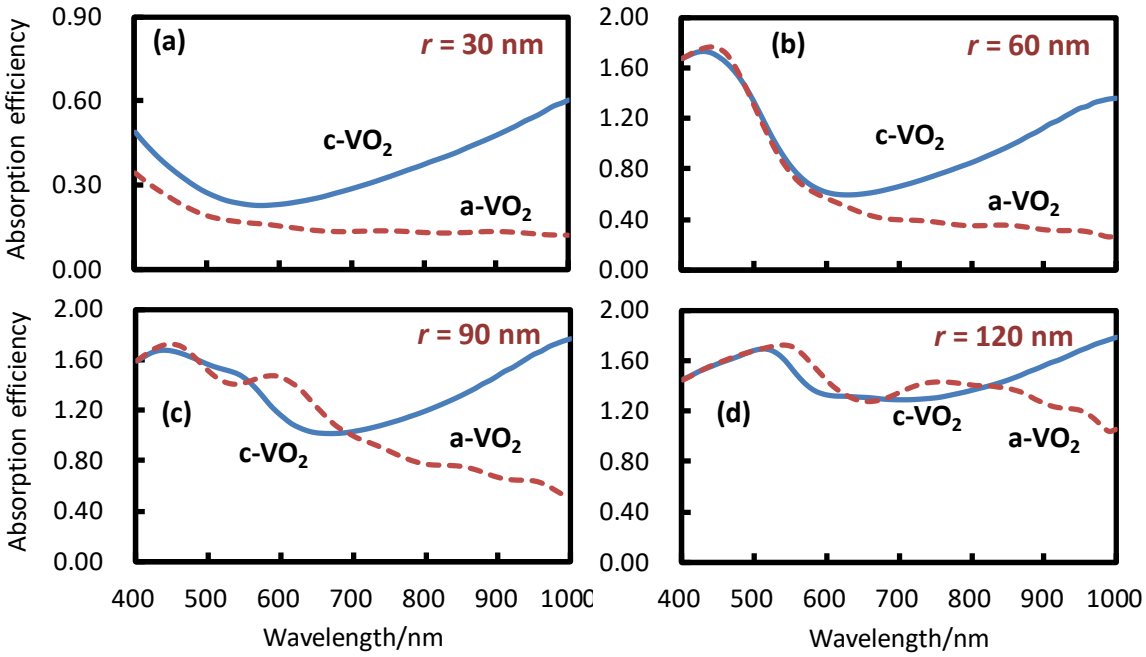

Fig. 2 Absorption efficiency of a-state and c-state VO_2 nanosphere with radius (a) *r* = 30 nm; (b) *r* = 60 nm; (c) *r* = 90 nm; (d) *r* = 120 nm.

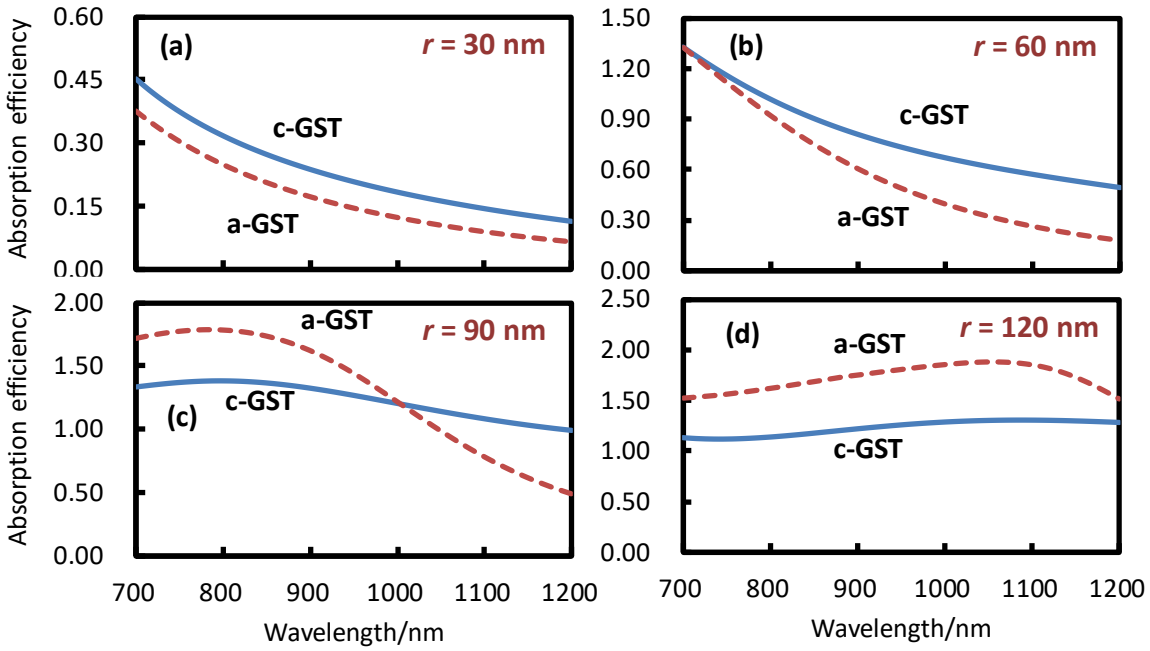

Fig. 3 Absorption efficiency of a-state and c-state GST nanosphere with radius (a) *r* = 30 nm; (b) *r* = 60 nm; (c) *r* = 90 nm; (d) *r* = 120 nm.

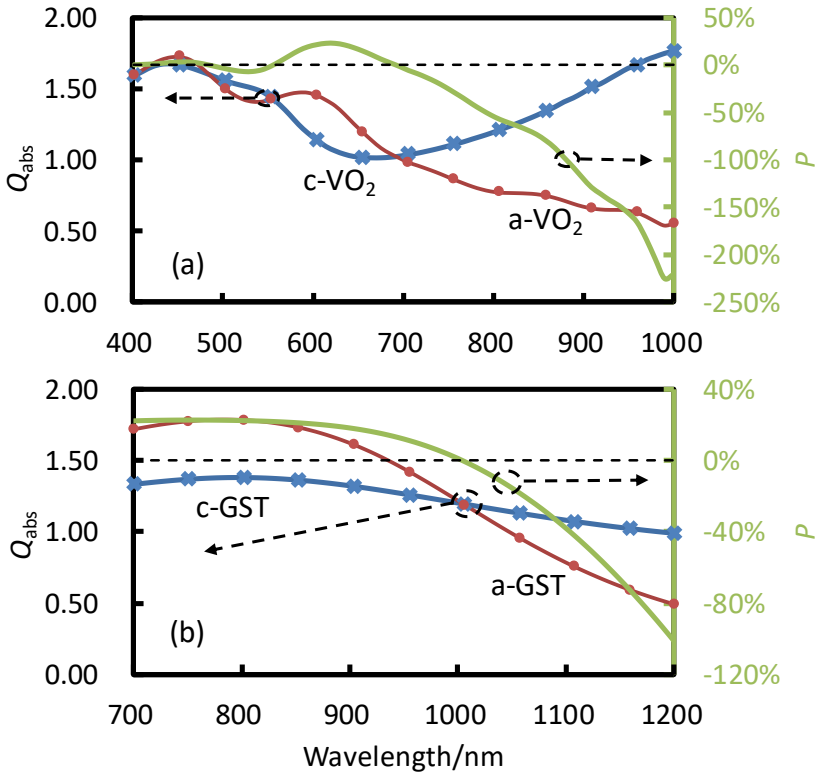

Fig. 4 Optical properties of (a) VO_2 and (b) GST nanospheres with *R* = 90 nm at amorphous and crystalline states.

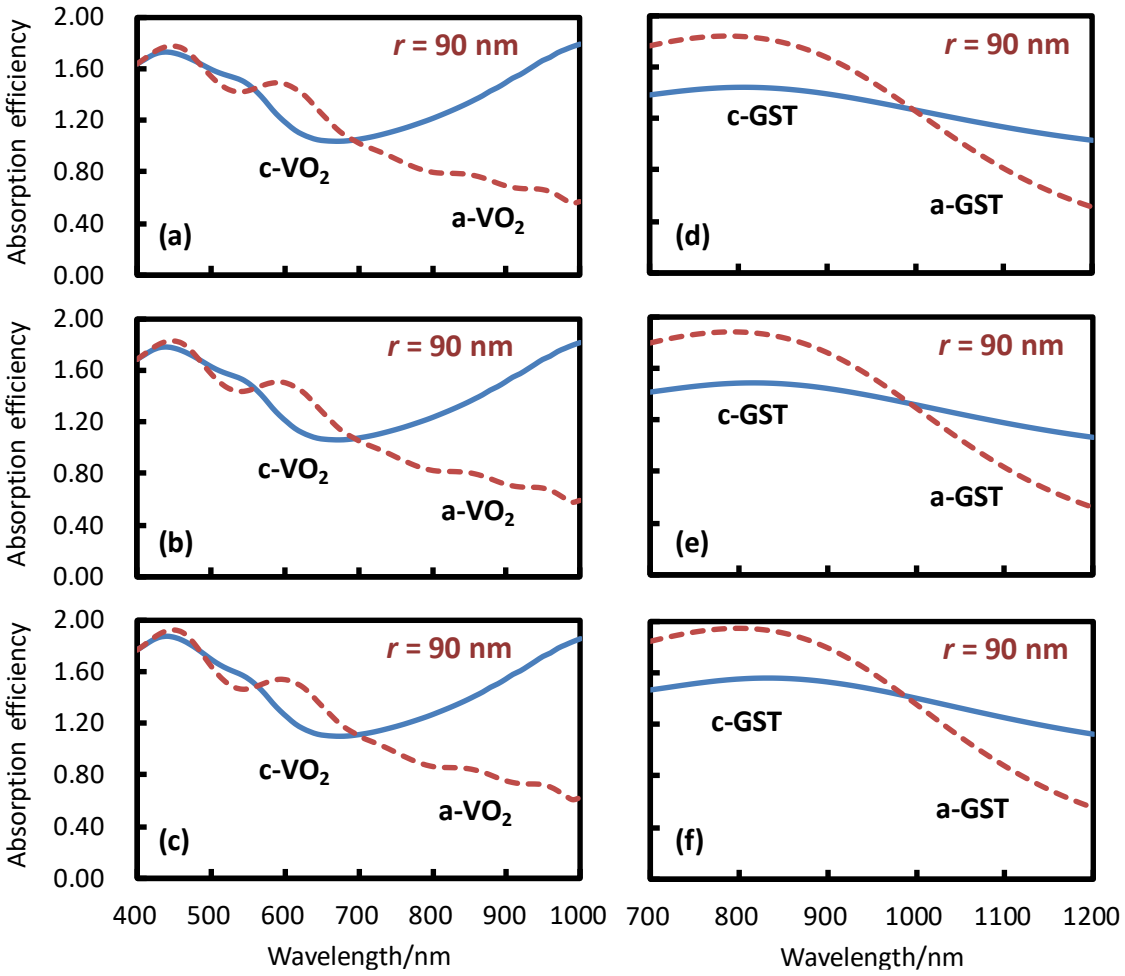

Fig. 5 Optical properties of VO_2 (a-c) and GST (d-f) nanoshells at amorphous and crystalline states with shell thickness: (a) 5 nm; (b) 10 nm; (c) 20 nm; (d) 5 nm; (e) 10 nm; (f) 20 nm.

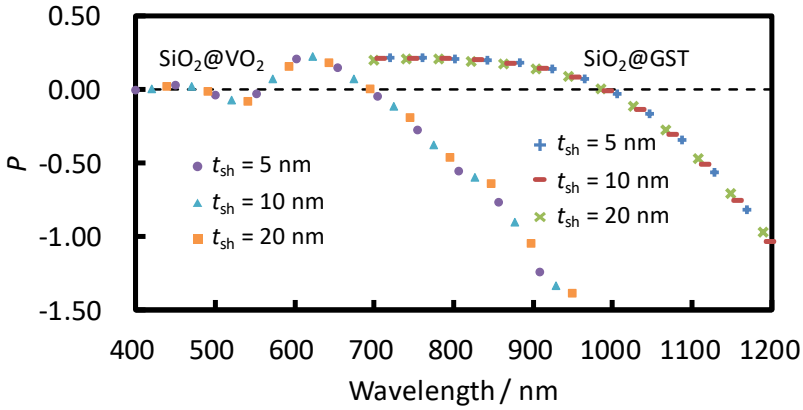

Fig. 6 Figure of merit *P* as a function of wavelength for different shell thickness t_{sh}.

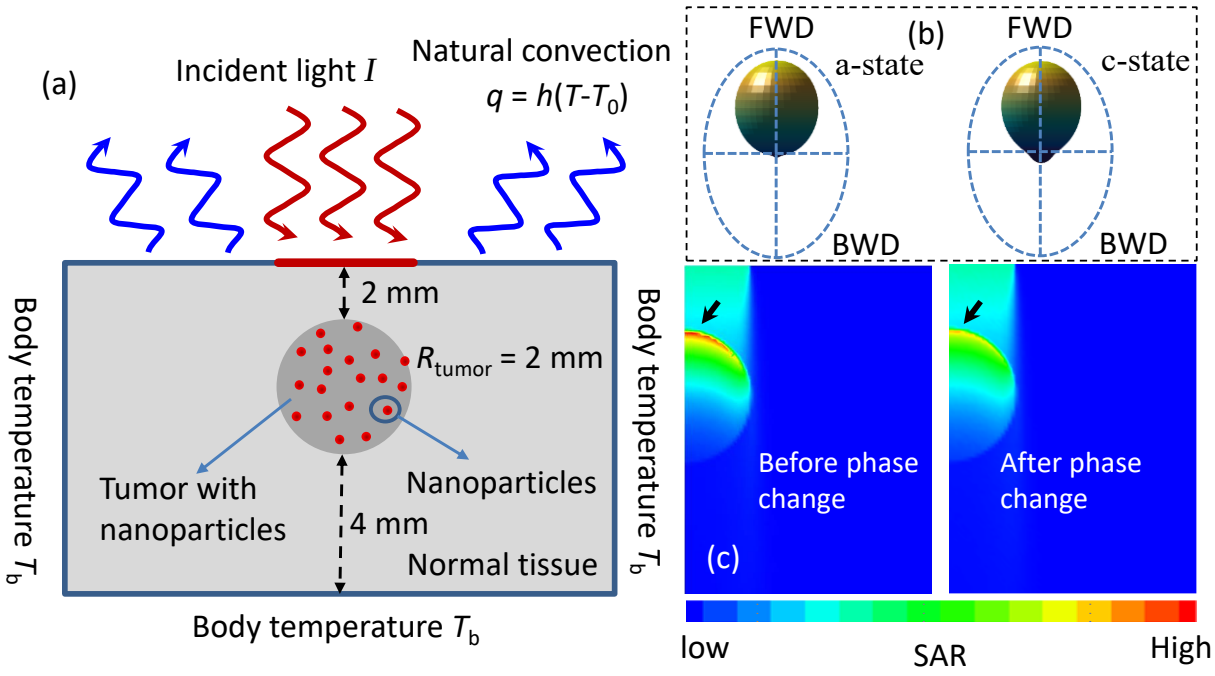

Fig. 7 SAR distribution in tumor. (a) Geometric model and boundary conditions for light and heat transfer during photothermal therapy; (b) radiation patterns of a-state and c-state VO_2 nanospheres with radius R = 90 nm. FWD and BWD mean forward and backward directions, respectively; (c) SAR distributions in tumorous area embedded with a-state and c-state nanospheres.

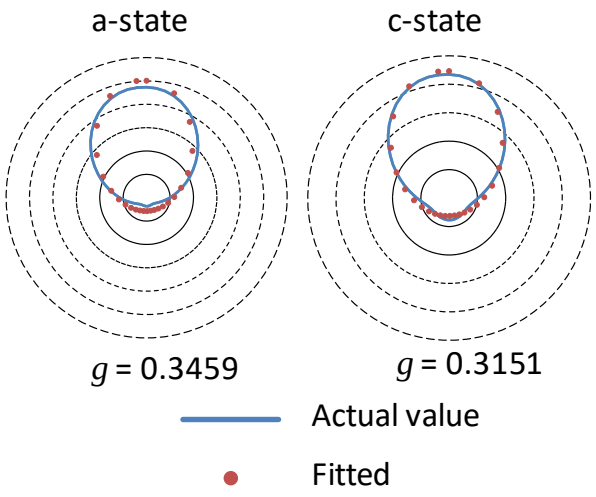

Fig. 8 Fitted results of H-G function and the radiation pattern of a-state and c-state VO_2 nanospheres with radius R = 90 nm.

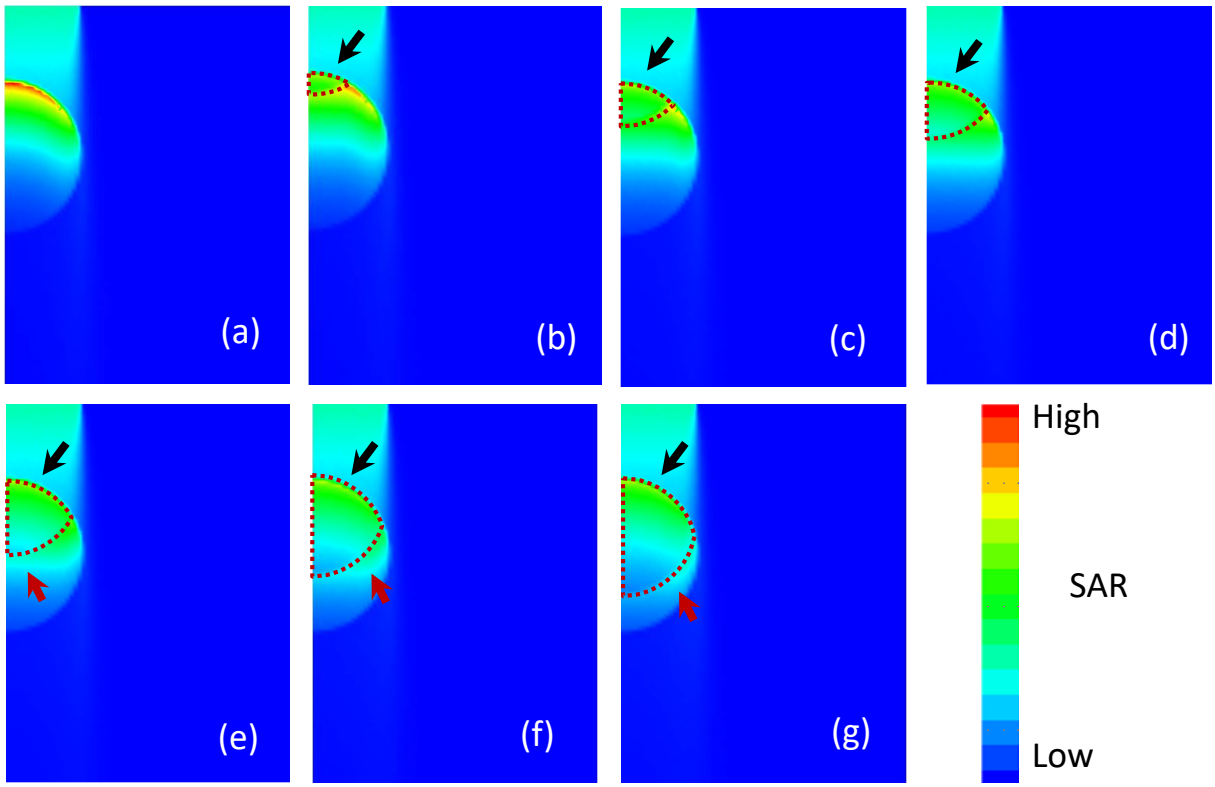

Fig. 9 SAR distributions for different sizes of high temperature zone. The high temperature zone is loaded with c-state nanoparticles and the rest part of the tumor is loaded with a-state nanoparticles.

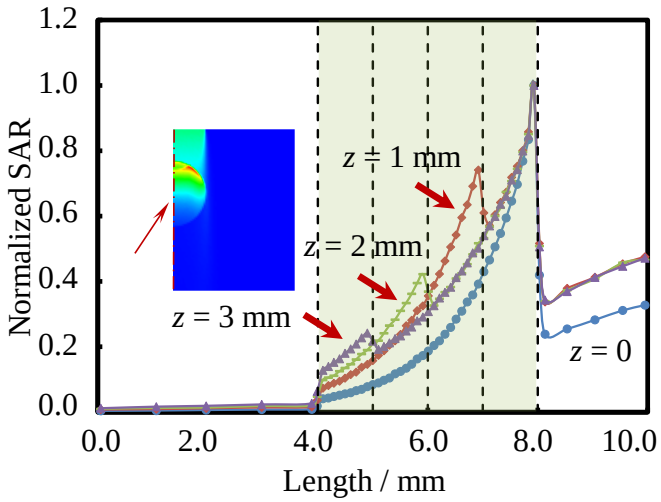

Fig. 10 SAR distributions along the center line of the model for different sizes of high temperature zone. *z* = 1, 2, and 3 mm means the hypothetical high temperature circle moving downward for 1, 2, and 3 mm, respectively.

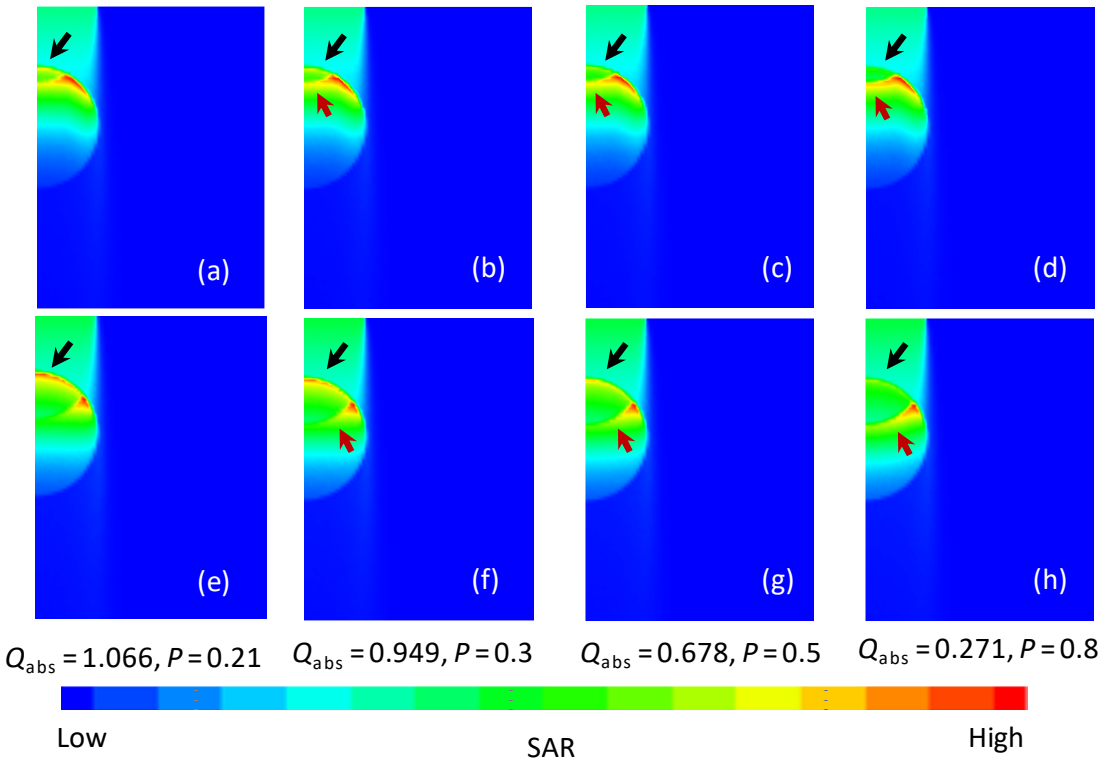

Fig. 11 SAR distribution for different absorption cross section of c-state nanoparticles: (a-d) *z* = 1 mm; (e-h) *z* = 1.5 mm.

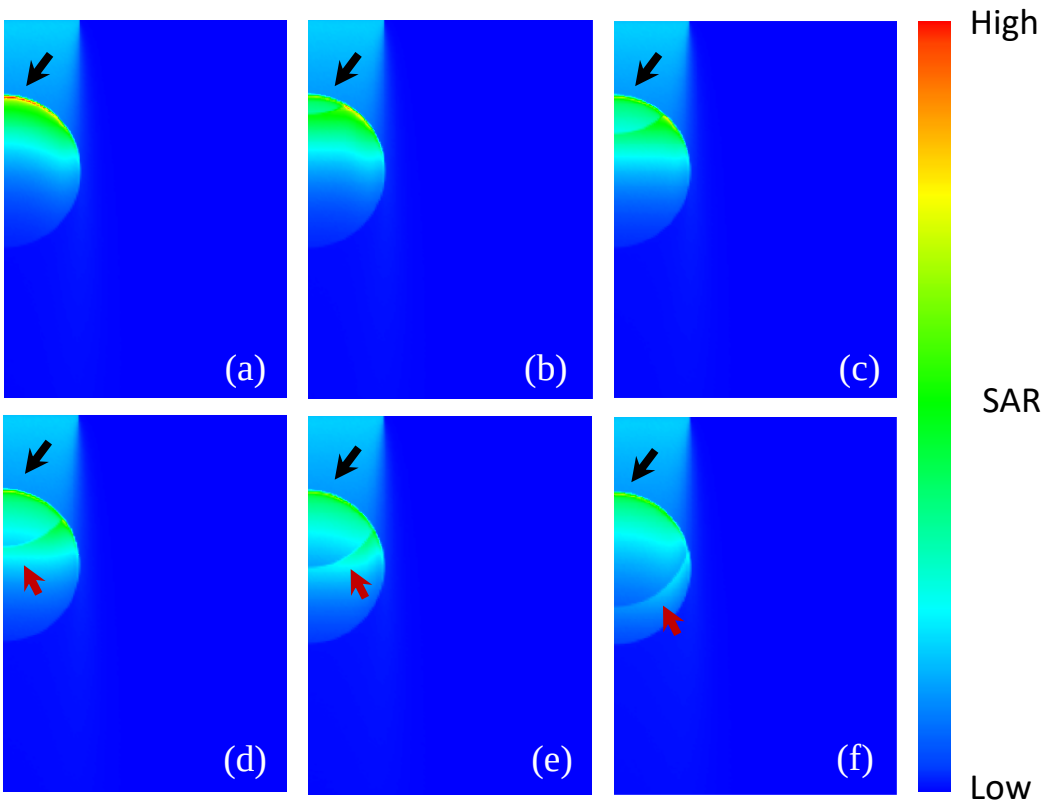

Fig. 12 SAR distributions for different sizes of high temperature zone for breast tumor.

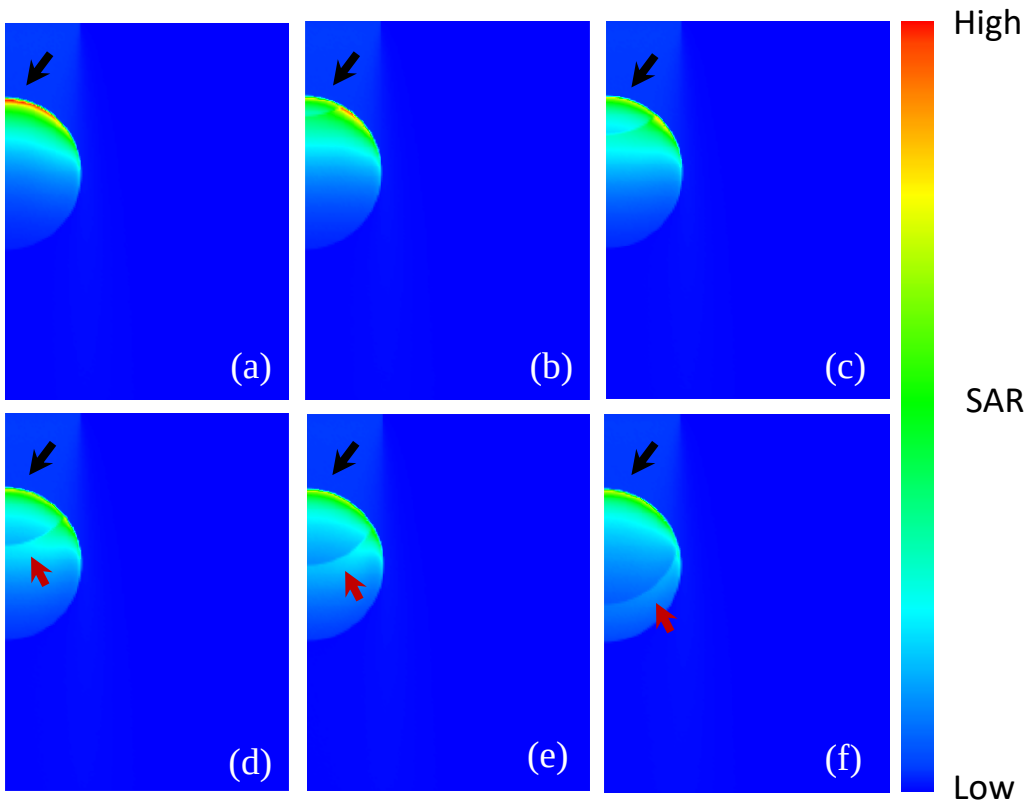

Fig. 13 SAR distributions for different sizes of high temperature zone for prostate tumor.

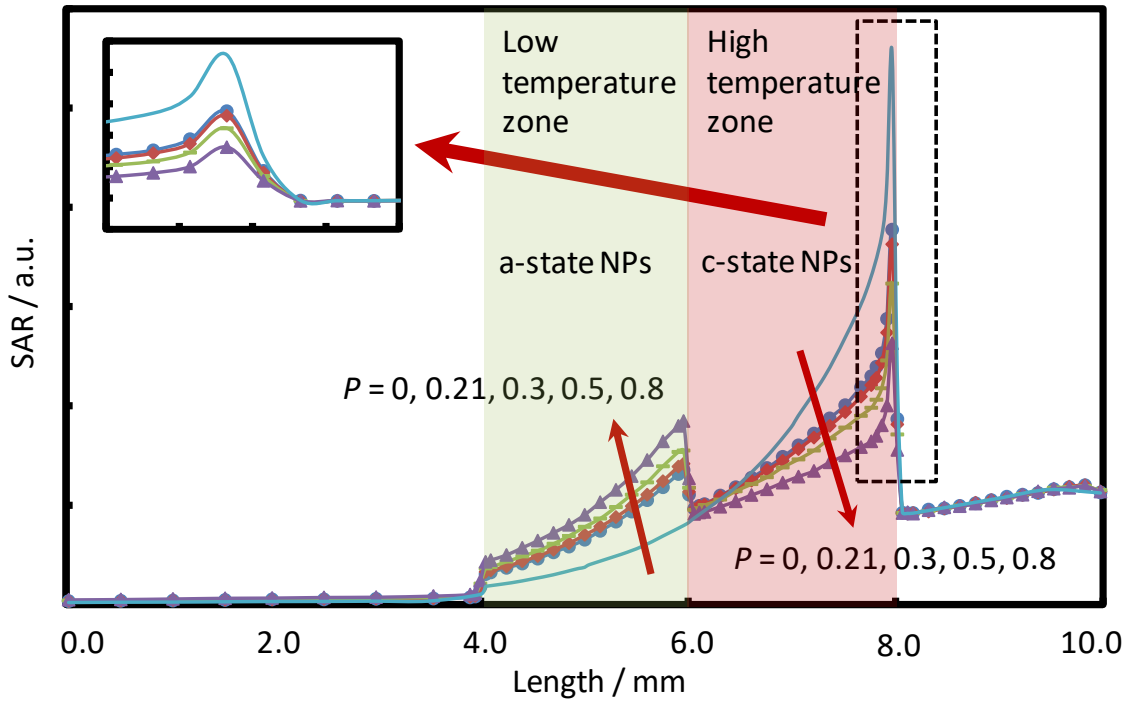

Fig. 14 SAR distributions along the center line of the model for different values of *P*.

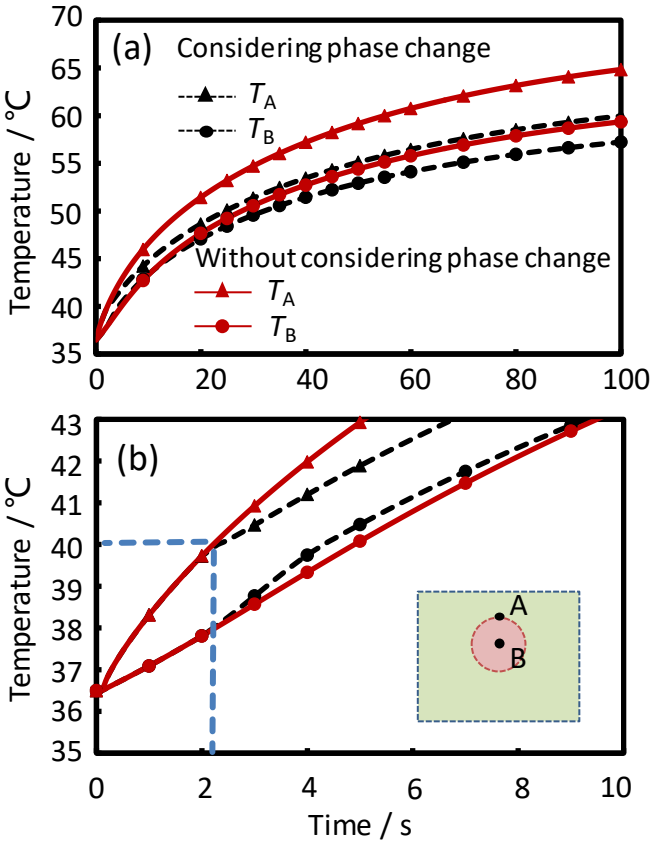

Fig. 15 Temperature profiles of two points inside tumor with and without considering phase change of embedded nanoparticles. Laser power density is set as 2.0 x 10^4 W/m^2.

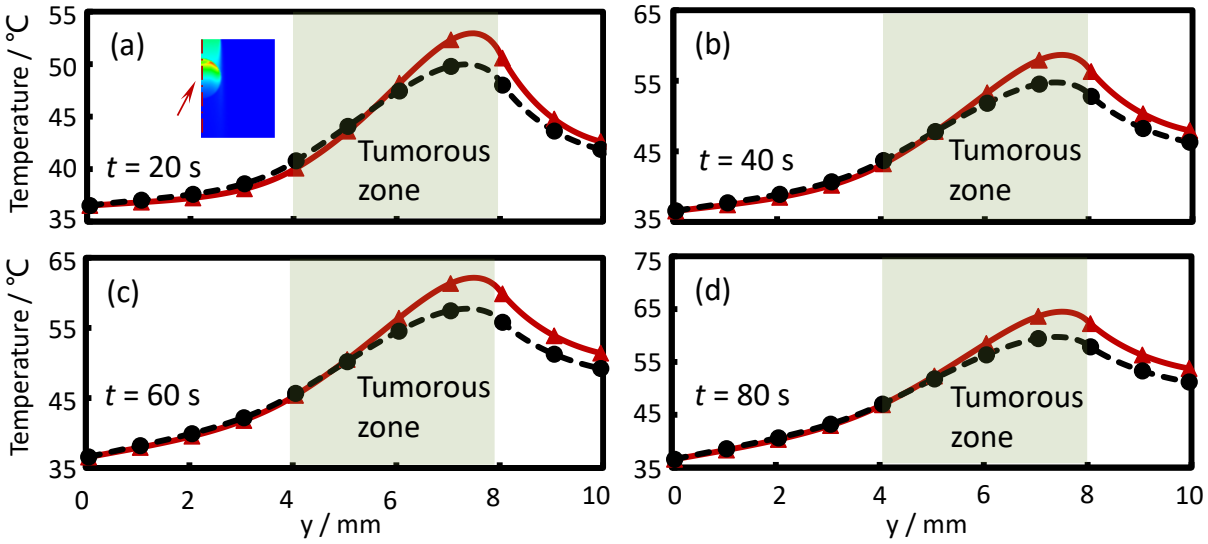

Fig. 16 Temperature distribution along the center line of the model at different time: (a) *t* = 20 s, (b) *t* = 40 s, (c) *t* = 60 s, (d) *t* = 80 s. The red solid lines are the temperature profile without considering the optical phase change of nanoparticles and the black dashed lines are the temperature profiles considering the optical phase change of nanoparticles.

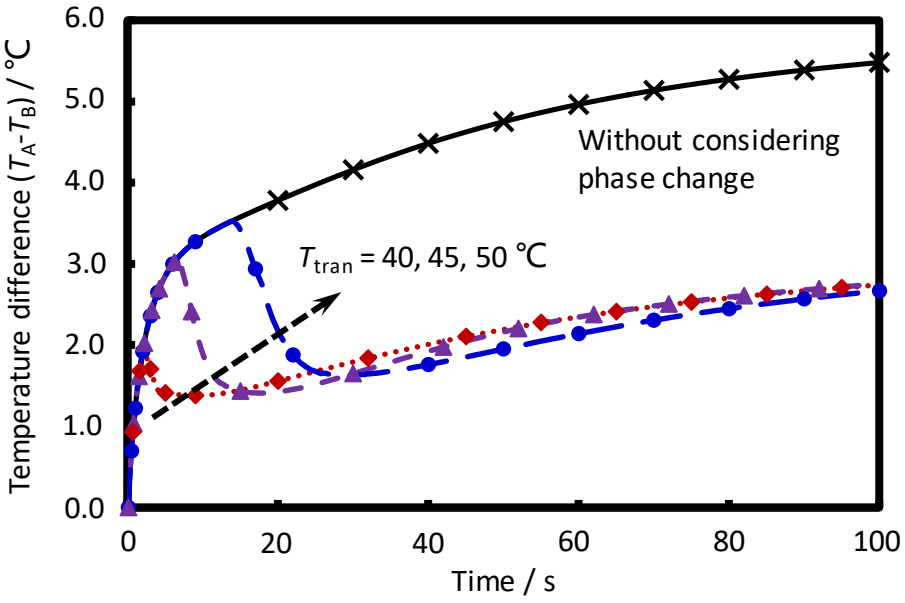

Fig. 17 Temperature difference between point A and B for different temperature of tissue which can induce the phase transition of nanoparticles.

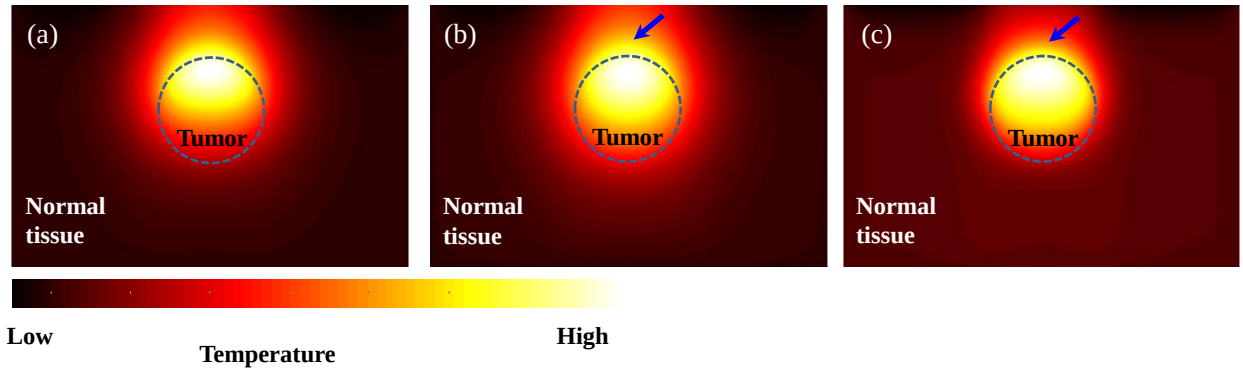

Fig. 18 Temperature distributions at 20 s for different values of *P* when the phase transition temperature is set as 40°C: (a) *P* = 0; (b) *P* = 0.21; (c) *P* = 0.8.

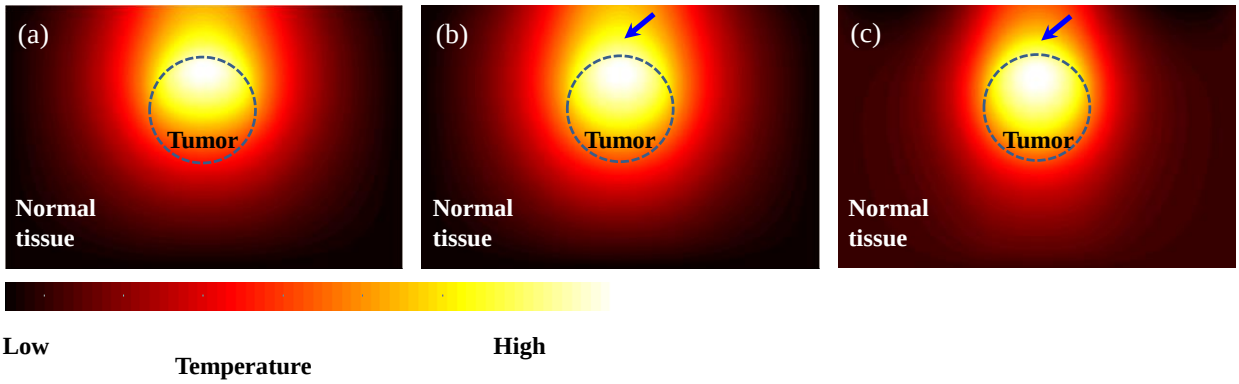

Fig. 19 Temperature distributions at 100 s for different values of *P* when the phase transition temperature is set as 40℃: (a) *P* = 0; (b) *P* = 0.21; (c) *P* = 0.8.